LAGRANGIAN APPROACH OF MODELLING THE PRODUCTION RATE OF CARBON NANOTUBES (CNTS) SYNTHESIS IN THE FCVD SYSTEM FOR SCALABILITY ANALYSIS

Ajani Jimoh Olanrewaju[a,b] Muhammad Thalhah Zainal[*c, d], Mohd Fairus Mohd Yasin[a, b], Norikhwan Hamzah [a, b]

[a]Department of Thermo-Fluids, Faculty of Mechanical Engineering, Universiti Teknologi Malaysia, 81310 UTM Johor Bahru, Malaysia.
[b]High Speed Reacting Flow Laboratory (HiREF), Universiti Teknologi Malaysia, 81310 UTM Johor Bahru, Malaysia.
[c]Department of Mechanical Precision Engineering (MPE), Malaysia-Japan International Institute of Technology (MJIIT), Universiti Teknologi Malaysia, Kuala Lumpur
[d]Takasago Thermal Environmental Systems (TTES) Research Laboratory, Malaysia-Japan International Institute of Technology (MJIIT), Universiti Teknologi Malaysia, Kuala Lumpur

[*]Corresponding Email: mthalhah@utm.my

Article history
Received
30th August 2025
Revised
22nd January 2026
Accepted
22nd January 2026
Published
2nd June 2026

ABSTRACT

Flame-assisted chemical vapour deposition (FCVD) is regarded as an effective method for synthesising carbon nanotubes at relatively low cost. Large-scale production of carbon nanotubes via FCVD is crucial to fully realize the technique's potential for creating nanomaterials for industrial uses. The absence of a comprehensive model for scaling up CNT synthesis in previous studies highlights the need for further development. Therefore, this research develops a baseline model for scaling up the synthesis process. It examines the factors leading to the decline in CNT yield as bead mass increases—specifically, fluidisation intensity, which depends on particle velocity, average growth temperature, and methane concentration—using a coupled computational approach combining computational fluid dynamics (CFD) and particle–scale modelling. In this method, the flow domain temperature was initially set at 500°C, and the substrate was fluidised at varying nitrogen shield gas flow rates across bead masses from 10 g to 25 g for scalability analysis. A discrete phase model (DPM), integrated into ANSYS Fluent CFD software and coupled with the Lagrangian framework, was used to track particle trajectories, gather data, and perform analysis. The CFD results were treated as inputs to the growth rate model for predicting CNT growth. The CNTs produced over a 10-minute growth period indicate the respective production rate for each bead mass. The study demonstrates that increasing fluidisation intensity from 11 to 14 slpm and bead mass from 10 to 25 g causes a decrease in temperature from 1200 to 1000 K. The velocity magnitude, which represents fluidisation intensity, rises from 0.017 to 0.02 m/s. Conversely, methane concentration peaks at the highest temperature, which occurs at the lower bead mass of 10 g. Notably, this high methane concentration at elevated temperatures highlights its essential role in methane decomposition.

Keywords: *Carbon nanotube synthesis, Lagrangian approach, production rate, FCVD, computational fluid dynamics, growth rate mo*del.

1.0 INTRODUCTION

Carbon nanotubes (CNTs) have garnered significant interest in the nanomaterials research community due to their remarkable properties, including thermal conductivity exceeding that of diamonds, electrical conductivity surpassing that of copper, and mechanical strength exceeding that of steel [1, 2]. CNTs are expected to play a vital role in various emerging applications, and realising their full potential depends on developing efficient and affordable mass-production methods [3, 4]. Several synthesis techniques have been designed to produce CNTs, including chemical vapor deposition (CVD), arc discharge, laser ablation, flame synthesis, and flame-enhanced chemical vapour deposition (FCVD). While CVD is considered the most suitable manufacturing method, it demands significant energy input and lengthy processing times. Although flame synthesis shows promise for lower energy consumption, it is limited by poor control over synthesis and low yields [5-7]. Studies have shown that flame synthesis of carbon nanotubes (CNTs) is challenging due to difficulties in controlling CNT growth within heterogeneous flame environments [8-10]. Recent research has addressed this issue by developing a multi-scale model that combines computational fluid dynamics (CFD) with a CNT growth rate model, systematically linking flame structure concepts to predict CNT growth zones [1, 11].

A hybrid approach combining CVD and flame deposition has emerged as a viable alternative to enhance synthesis control and reduce energy consumption. [1-3]. A low-cost, quick, and sustainable production method is needed to address the limitations of energy-intensive chemical vapour deposition (CVD). Flame chemical vapour deposition (FCVD) offers a cost-effective method for synthesising carbon nanotubes (CNTs) with minimal energy consumption. Incorporating CVD furnaces into flame synthesis allows precise temperature regulation within the growth zone [4-6]. Spherical substrates, such as zirconia beads, offer a significant growth area with increased mobility, making them suitable for large-scale production. The fluidised bed chemical vapour deposition (FBCVD) technique is a scalable, relatively inexpensive method for producing high yields of CNTs. Recent developments in catalytic chemical vapour deposition (CCVD) demonstrate the advantages of using a fluidised bed reactor within the flame-assisted chemical vapour deposition (FCVD) system for commercial CNT manufacturing. [7, 8]. Despite its potential, the FCVD approach has received limited attention, especially concerning the influence of flame and furnace settings on CNT formation. Research on flame-assisted chemical vapour deposition (FCVD) for CNT growth remains limited, with earlier studies concentrating on aerosol-type substrates [5]. The effects of fluidisation, growth temperature, and methane concentration on CNT synthesis in the FCVD system require further investigation using computational fluid dynamics (CFD) for large-scale production.

Computational studies of carbon nanotube (CNT) synthesis in flame environments [12] emphasize the need for a multiscale model that combines computational fluid dynamics (CFD) with particle–scale modeling. This approach has effectively predicted CNT growth regions within flames, aligning well with experimental results. A related study using the same method successfully identified linear and quadratic relationships for the lower and upper boundaries of the CNT growth region in the mixture fraction space. A study by Muhammad Syafiq et al. [9] employed a similar multiscale approach, using a dispersed-phase model (DPM) within the CFD simulation to model the entrainment of catalyst particles during the flame synthesis of single-walled carbon nanotubes (SWCNTs) with aerosol catalysts. The study further predicted the growth rate of CNTs at each particle. Additionally, the effects of oxygen on SWCNTs were examined.

The author of [6] developed a computational model framework to capture the complex interplay of multiscale phenomena involved in the CVD technique. It was discovered that significant gas-phase reactions occur in mixed hydrocarbon feedstocks and that catalyst deactivation effects are substantial. The results also revealed that CNT growth is controlled by gas composition and transport, as well as temperature and catalyst properties [6]. In another study, catalytic chemical vapour deposition (CCVD) in a fluidized-bed

reactor was utilised to achieve continuous, large-scale production of high-quality carbon nanotubes (CNTs) [7]. A coupled computational fluid dynamics–population balance model (CFD-PBM) was employed to simulate CNT production, examining the effects of ethylene mole fraction, superficial gas velocity, and initial bed height on carbon yield. The results show that the simulated carbon yield and particle growth rate align well with experimental data. [8]. A recent study investigated the impact of carbon precursors on the growth regions of CNTs on nickel catalyst particles within an ethylene inverse diffusion flame [9]. The research employed a CNT growth rate model to predict CNT length and growth regions, using empirical data on flame temperature and species composition. Various precursor combinations were tested as inputs to the growth rate model to identify the dominant precursor for CNT growth. The findings emphasised the importance of acetylene and carbon monoxide, with acetylene playing a significant role [9].

A recent computational study [10] developed a modeling framework that combines density functional theory, microkinetic modeling, and computational fluid dynamics to predict CNT growth in chemical vapor deposition (CVD) processes. The model successfully captures the complex interactions among gas-phase reactions, surface kinetics, and catalyst properties, providing valuable insights into CNT growth dynamics [10]. Others conducted numerical simulations to examine the competition between CNT growth and soot formation in a laminar inverse diffusion flame, revealing that the ratio of the carbon bulk diffusion rate to the soot nucleation rate is a better indicator of CNT growth regions than the carbon bulk diffusion rate alone [11]. These findings offer guidance on optimizing flame conditions to reduce soot formation and enhance CNT growth [11].

It is evident from current studies that a reliable model for predicting CNT production rate for upscaling in FCVD is yet to be developed. Therefore, the present study aims to establish a baseline model for FCVD upscaling analysis, serving as a predictive tool for large-scale carbon nanotube production in such systems. Factors influencing CNT production rate and yield, which are difficult to identify experimentally and also limit the scalability, are thoroughly examined.

2.0 EXPERIMENTAL PROCEDURE

Figures 1(a) and (b) show the actual experimental setup and its schematic diagram, respectively. The dashed region in Figure 1(a) represents the simulation domain of the FCVD synthesis system, which comprises a burner, a heater, a quartz tube enclosure containing a stack of ceramic beads on a wire mesh, and a collector tube. Premixed fuel flows through the central tube of the burner, which has a 12.6 mm diameter. In comparison, nitrogen shield gas passes through a 2 mm-diameter concentric annular tube to facilitate fluidisation. The simulated region includes the burner, wire mesh, and beads, which are enclosed within the quartz tube of the furnace. To achieve a suitable
growth temperature for CNTs, the furnace was maintained at 500°C.

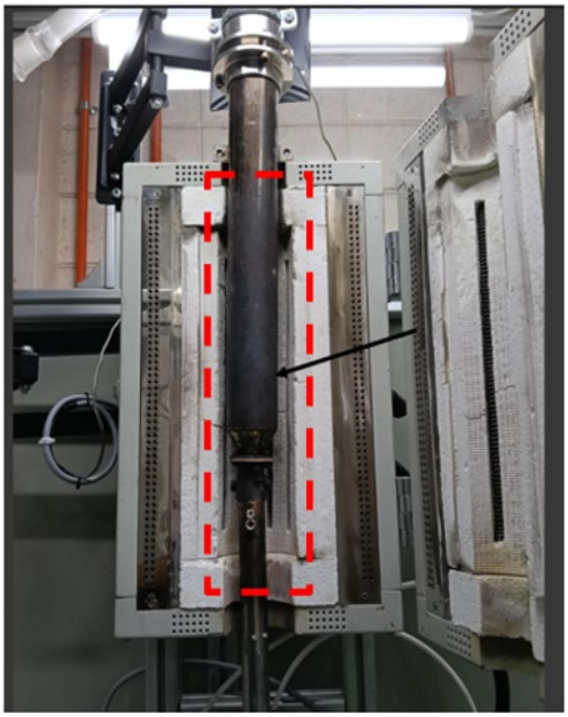

Figure 1 (a) Actual rig picture

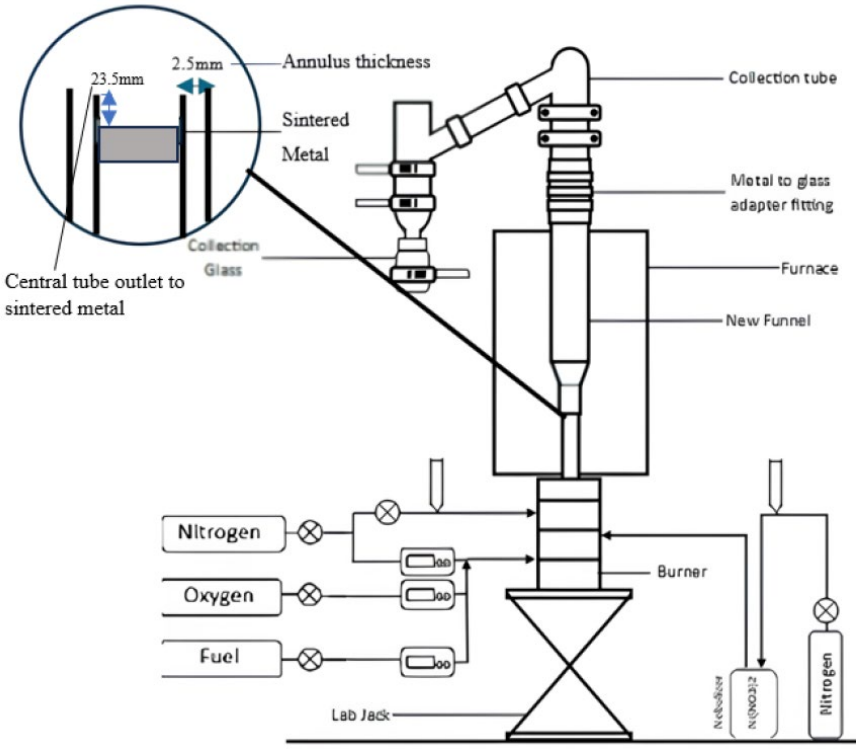

Figure 1 (b) schematic diagram of the rig

The present study simulates CNT growth at a height of 70 mm above the burner (HAB). This location of interest corresponds to the experimental results obtained at 70 mm HAB. Zirconia beads with a diameter of 0.3 mm were fluidized at different masses, as shown in

Table 1. Each condition was tested for 10 minutes. The premixed fuel entering the burner consisted of methane at 0.4 slpm, oxygen at 0.445 slpm, and nitrogen at 0.8 slpm, resulting in an equivalence ratio. ϕ of 1.8. The entire rig enclosure was connected to a collection tube designed for efficient CNT collection.

Table 1: Experimental conditions employed as input for numerical calculations

Case	Mass flow rate of the nitrogen shield gas, slpm	Mass of beads, g	Measured production rate, mg/min	Methane mass flow rate, slpm	Minimum nitrogen gas flow rate, slpm	Oxygen mass flow rate, slpm
1	11	10	1.2	0.4	0.8	0.445
2	12	15	0.9	0.4	0.8	0.445
3	13	20	0.7	0.4	0.8	0.445
4	14	25	0.8	0.4	0.8	0.445

3.0 COMPUTATIONAL PROCEDURE

3.1 Computational Fluid Dynamics (CFD) Simulation of the FCVD System

A numerical simulation was performed using Computational Fluid Dynamics (CFD) to visualize the flow field resolution within the computational domain, as shown in Figure 2. Conservation equations of mass, momentum, energy, and chemical species under steady-state conditions, as indicated by Equations 1 – 4, respectively. Turbulence modelling was incorporated using the standard. $k-\omega$, 2-equation model. The Reynolds-Averaged Navier-Stokes (RANS) equations were employed to solve the governing equations, with a species transport model. The CFD solver suitable for compressible and reacting flows was employed in the present study., Equation (1) describes the continuity equation, which expresses mass conservation in a control volume, relating to fluid density (ρ) and velocity (u). Here, i denotes the spatial direction of the flow based on the i =1,2, and 3 conventions for fluid velocity in the x, y, and z directions, respectively. The momentum equation (Equation 2) determines the velocity distribution within the flow domain, considering the normal stress. (σ_{ij}), viscous force (τ_{ij}), and external forces (Y_k) and ($f_{k,j}$) Species conservation equation (Equation 3) governs chemical species behaviour, solving mass fraction (Y) of species k, considering diffusion velocity ($V_{k.i}$) and production rate ($\dot{\omega}_k$) through chemical reactions. Variables T, c_p, h_k and k in Equation (4) are the combustion gas temperature, specific heat capacity, and specific enthalpy of species k, respectively [12-14] .

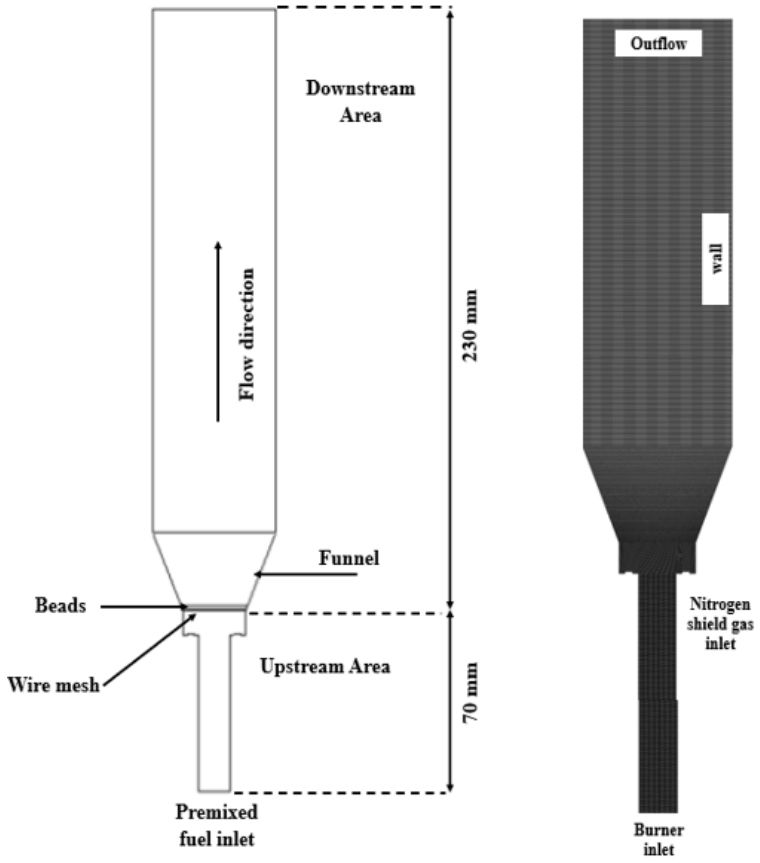

Figure 2: Planar two-dimensional computational domain

$$\frac{\partial \rho}{\partial t} + \frac{\partial \rho u_i}{\partial x_i} = 0 \quad (1)$$

$$\frac{\partial \rho u_i}{\partial t} + \frac{\partial \rho u_i u_j}{\partial x_j} = \frac{\partial \sigma_{ij}}{\partial x_j} + \frac{\partial \tau_{ij}}{\partial x_i} + \rho \sum_{k=1} Y_k f_{k,j}, \; i = 1,2,3 \quad (2)$$

$$\frac{\partial \rho Y_k}{\partial t} + \frac{\partial}{\partial x_i}\left(\rho\left(u_i + V_{k,i}\right)Y_k\right) = \dot{\omega}_k \quad (3)$$

$$\rho \frac{\partial T}{\partial t} = \rho \frac{1}{2}\left(\frac{\partial^2 T}{\partial {x_i}^2} + \frac{1}{c_p}\frac{\partial c_p}{\partial x_i}\frac{\partial T}{\partial x_j}\right) - \frac{1}{c_p}\sum_{k=1}^{n} h_k \dot{\omega}_k \quad (4)$$

A simple semi-implicit algorithm was employed to couple velocity and pressure. The governing equations are discretised using the second-order upwind scheme for pressure. Similarly, the second-order upwind scheme was also applied to the momentum, turbulent kinetic energy, specific dissipation rate, and energy equations. The spatial discretisation of gradient terms was handled using the Least Squares Cell-Based (LSCB) method, which is known for its relatively short computational time [15, 16].

The computational work was based on the existing FCVD setup, simplified into a two-dimensional planar domain, as shown in Figure 2. The geometry includes the upstream

section, which extends from the burner to the wire mesh location and is 70 mm above the burner inlet in this setup. The zirconia beads serve as substrates for CNT growth sites and undergo catalyst deposition during the initial stage of CNT development. The beads are densely packed on the wire mesh within the funnel and weigh between 10 and 25 grams, in 5-gram increments. The downstream area is the region beyond the beads, extending to the outlet over a distance of 230 mm. The boundary conditions listed in Table 1 are applied at the inlet. The inlet boundary temperatures for both the burner and the nitrogen gas are 300 K. In this study, the nitrogen flow rate controls fluidization intensity, primarily in the upstream section where primary combustion occurs. A no-slip condition is applied at the wall boundaries, and a pressure outlet condition is used at the outlet boundary. The zero-gradient pressure condition ensures the boundary adopts the value of the nearest adjacent cell. The mesh is finely structured, consisting of 204,000 cells.

The Discrete Phase Model (DPM) employs a Lagrangian approach to track individual particles within a fluid [17, 18]. In this study, DPM is used to represent beads, enabling visualisation of their flow and extraction of trajectory-based data. The temperature and combustion species data from individual trajectories serve as input parameters for the growth rate model, which predicts the CNT growth rate. Conversely, the Eulerian frame of reference is fixed in space, describing the motion of a fluid or gas in terms of velocity and position at a given point. The Lagrangian frame analyzes the Discrete Phase Model (DPM) by tracking individual particles as they move through the continuous flow fields computed in the Eulerian frame. Creating an injection type involves defining initial conditions for discrete particles or droplet releases [19, 20]. Surface injection means each surface facet releases the particle stream. The setup interface specifies properties such as the beads' temperature, mass, density, and diameter.

In ANSYS FLUENT, the material representing beads is anthracite. The diameter distribution is uniform, and the particles are inert. Lagrangian data were post-processed as parcels, each representing a group of particles with similar trajectories. A total of 500 parcels were generated and exported to MATLAB to calculate the average temperature and species values using Equations 5 and 6, respectively.

$$T_{avg} = \frac{1}{n}\sum_{i=1}^{n} T_i, \quad where\ i = 1,2,3 \dots \dots n \tag{5}$$

$$C_{avg} = \frac{1}{n}\sum_{j=1}^{m} C_i, \quad where\ i = 1,2,3 \dots \dots m \tag{6}$$

3.2 Formulation of Predicted Production Rate from CNT Growth Rate Model (GRM)

The CNT growth rate model (GRM) developed by [9, 19, 20] was employed in the present study as the starting point to derive the predicted production rate. Ordinary differential equations (ODEs) that constitute the GRM describe the physical processes of carbon-catalyst interplay in the build–up of CNTs, as defined by Equation (7). Thus, the numerical solution of Equation (7) is used to calculate the CNT length and growth rate, as shown in Equations (8) and (9), respectively. The CNT growth rate could be obtained by differentiating Equation (9) with respect to time, resulting in Equation (10).

$$\frac{dn_1}{dt} = F_{c1} - \frac{n_1}{\tau_{res}} - R_{d,out} - \sigma_x D_s n_1 n_x - (i+1)\sigma_i D_s n_1 n_i - \phi_{c1}\left(\frac{n_{p1}+n_{p2}}{\alpha_m n_m A_{np}}\right) \tag{7}$$

$$L = \left[\frac{1}{a_c C^*}\sqrt{\frac{D_b}{\pi}}\right] \times \int_0^t \frac{n_1}{\sqrt{t}}\,dt \tag{8}$$

$$G = \frac{n_1}{a_c C^*}\sqrt{\frac{D_b}{\pi t}} \tag{9}$$

$$A_{active} = N a_i\ (m^2) \tag{10}$$

The average CNT length L as computed by Equation (7), depends on the average temperature, T_i, and the average carbon precursor concentration, C_i. Variable N indexes the parcels and j indexes the particles within the parcel with$j = 1,2,3 \ldots . m$ .The averages of the various instances of the temperature and species are calculated as expressed in Equation (7). CNT growth rate ($GR = \frac{L}{T}$) is predicted by the growth rate model as the length of the CNTs per unit time. On the other hand, the production rate is measured experimentally. The growth rate can be compared to the experimental production rate by multiplying it by the substrate surface area and the CNT density. The resulting predicted production rate. PPR and its average PPR_{avg} are shown by Equations (8) and (9), respectively:

$$L = f(T_{avg}, C_{avg}) = \sum_{k=1}^{N} \frac{1}{m} \sum_{j=1}^{m} f(T_j, C_j)\,, j\ {}^{j=1,2,3.....m}_{k=1,2,3.....N} \tag{11}$$

$$PPR_i = \frac{L_i}{T_i} \times A_i \times \rho_i \tag{12}$$

$$PPR_{avg} = \frac{1}{n}\sum_{i=1}^{n} PPR_i\,, where\ i = 1,2,3 \ldots \ldots n \tag{13}$$

The predicted production rate is calculated as the product of the growth rate (length of CNTs per unit time, L/T), the spherical beads' surface area, and the published CNT density. The average production rate is determined by summing all parcel values, as shown in Equation 12. Each parcel contains 1055 particles at different locations. The active area of each parcel of beads is given by Equations (10) to (12), where $N, n,$ and a_i are the total number of active particles, the active particles, and the area, respectively.

$$A_{active} = N a_i\ (m^2) \tag{14}$$

$$= \sum_{i=0}^{K} n_i \tag{15}$$

$$a_i = \begin{cases} 1 & l_i > 0.7 L_{max} \\ 0 & l_i \le 0.7 L_{max} \end{cases} \tag{16}$$

The surface area where CNTs grow is referred to as the active area, while the remaining area is considered non-active. The active regions are determined by selecting areas greater than 70% of the maximum CNTs length (L_{max}), which serves as a value. The equation for active areas is defined as the area with the CNT length, indicating active regions, and for non-active areas with $l_i \le 0.7 L_{max}$. The surface area of the beads is calculated using the formula $4\pi r^2$ of a single bead, taken to be 0.3 mm in diameter. The bead density is reported as 1420 kg/m³, with a bead diameter of 0.3mm, as noted in [1, 12, 21].

The histograms in Section 5 show the probability distribution of key factors affecting the FCVD synthesis system, specifically velocity, methane concentration, and temperature. Each histogram displays a probability function, $P(x)$, shaped by a normal

distribution, offering insight into the likelihood of different values in the dataset. The x-axis represents the variable being measured (temperature, velocity, or methane concentration), while the y-axis shows the probability density. These visualizations enable a thorough understanding of how these variables interact and influence the system, facilitating further analysis and interpretation.

4.0 RESULTS AND DISCUSSION

4.1 Validation of the Production rate and the Outlet temperature

Validation tests were performed for the CFD and GRM simulations, as shown in Figures 4 (a) and (b). Figure 4(a) shows the temperature validation of the FCVD system at a constant furnace temperature of 500 °C. It presents the average temperature derived from the temperature distributions across the four cases. The predicted average temperature is compared to the actual measurement taken outside the growth chamber at the exact location where the thermocouple used for the experimental data was positioned.

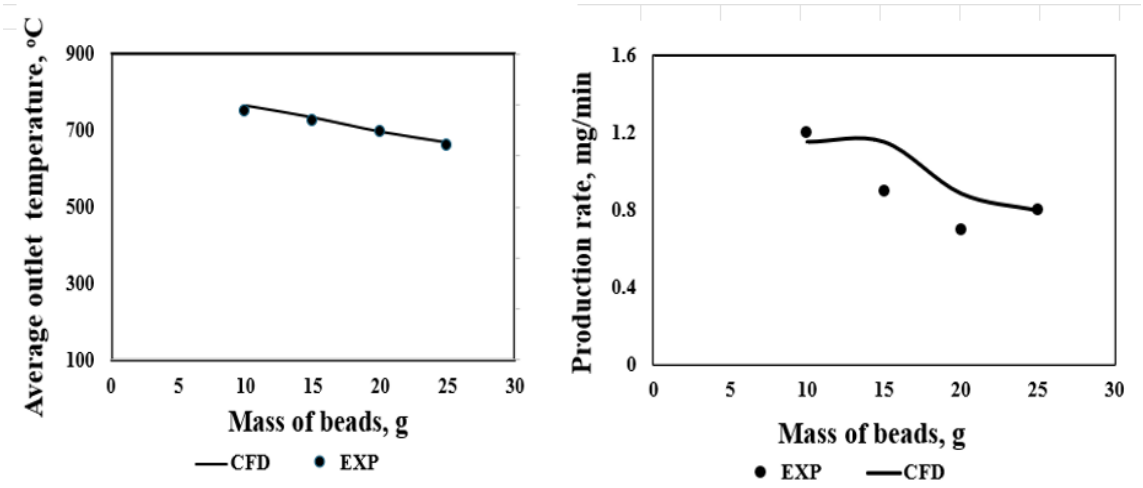

Figure 3: (a) Average temperature validation (b) Production rate validation

The results show reasonable agreement in both trend and magnitude across all four cases. This trend confirms the flow behaviuor with increasing bead mass. As the beads' mass increases, more vigorous fluidization is required. This increased energy input results in a higher flow of cold inert gas, leading to a decrease in furnace temperature as bead mass increases.

The validation of the production rate involved comparing experimental results with predicted values. As shown in Figure 4(b), the calculated production rate closely matches the experimental data at bead masses of 10 g and 25 g.

However, the predicted growth rate from the coupled simulation overestimated the production rates at bead masses of 15 g and 20 g by 13%. The decrease in the expected production rate is due to the growth rate model's response to the decreasing furnace temperature distribution as bead mass increases. Validating the production rate here provides a baseline for future scalability studies. Notably, the model showed an initial increase in production rate at lower bead masses, followed by a decline at higher masses, which aligns with the pattern observed in experimental investigations.

4.2 Relationship between the Predicted Production Rate and the Growth

Since the predicted production rate (PPR) is a function of the growth rate (GR), the PPR is directly proportional to the GR. Figure 3 shows the linear relationship between PPR and GR, described by the linear relationship shown in Equation (18) with R^2value of 0.9766. Based on Equation (18), the slope takes a value of 2.6253, and the y-intercept is 0.2168.

$$PPR \propto GR \Rightarrow PPR = k \times GR \tag{17}$$

$$y = 2.6253x + 0.2168 \tag{18}$$

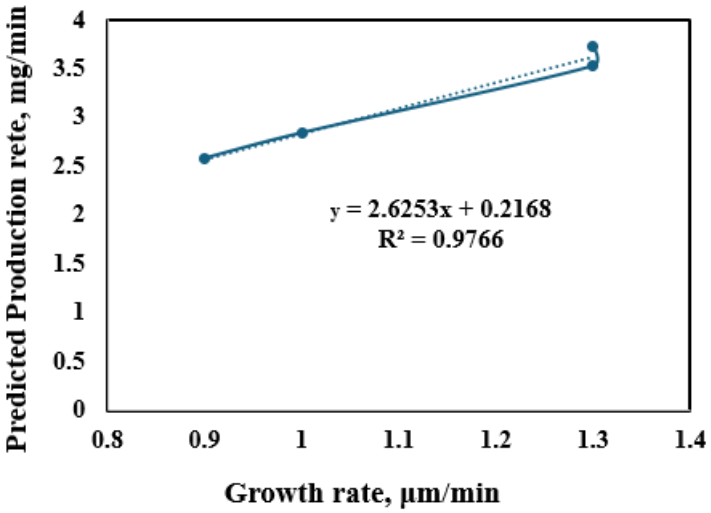

Figure 4: Relationship between the PPR and GR

Based on dimensional analysis, the slope indicates that for each unit increase in growth rate (µm/min), the predicted production rate increases by approximately 2.63 mg/min. Thus, Figure 3 establishes a clear linear correlation between the predicted production rate and the growth rate, demonstrating that CNT production can be effectively estimated from the modeled growth rate.

By performing dimensional analysis to balance the equation relating the growth rate to the predicted production rate, the slope, k in mg/mg, is obtained.

Figure 3 illustrates the relationship between the predicted production rate (PPR) and the growth rate (GR) to establish a linear correlation that, for every 1 mg of carbon nanotubes, there will be 2.623 μm length of the carbon nanotubes. This is a unique discovery that has not been previously documented in the literature.

4.3 Fluidization intensity determined by the average velocity

The results shown in Figure 5 indicate a nearly constant fluidization intensity, determined by the velocity magnitude across all four cases (a-d). The velocity magnitude remains relatively stable, with most particles moving between 0.005 and 0.02 m/s, unaffected by the increase in bead mass. The velocity rises with increased fluidization from 11 to 14 slpm but there are no significant changes in its intensity as the bead mass increases from 10 g to 25 g. The growth temperature decreases as fluidization increases, but this does not significantly impact the production rate. Since the effects of fluidization are subtle in the four cases shown in Figure 5, and because the decreasing average growth temperature—which leads to a drop in production rate—suggests that the main factor behind the reduction in production may be

the temperature regime within the growth chamber. In other words, the influence of velocity magnitude is minimal in increasing production, as it only slightly increases from 0.005 m/s to about 0.02 m/s across the four cases. This indicates a steady velocity regime as the bead mass increases from 10 g to 25 g, making it unlikely to explain the decline in production rate observed in the experimental results.

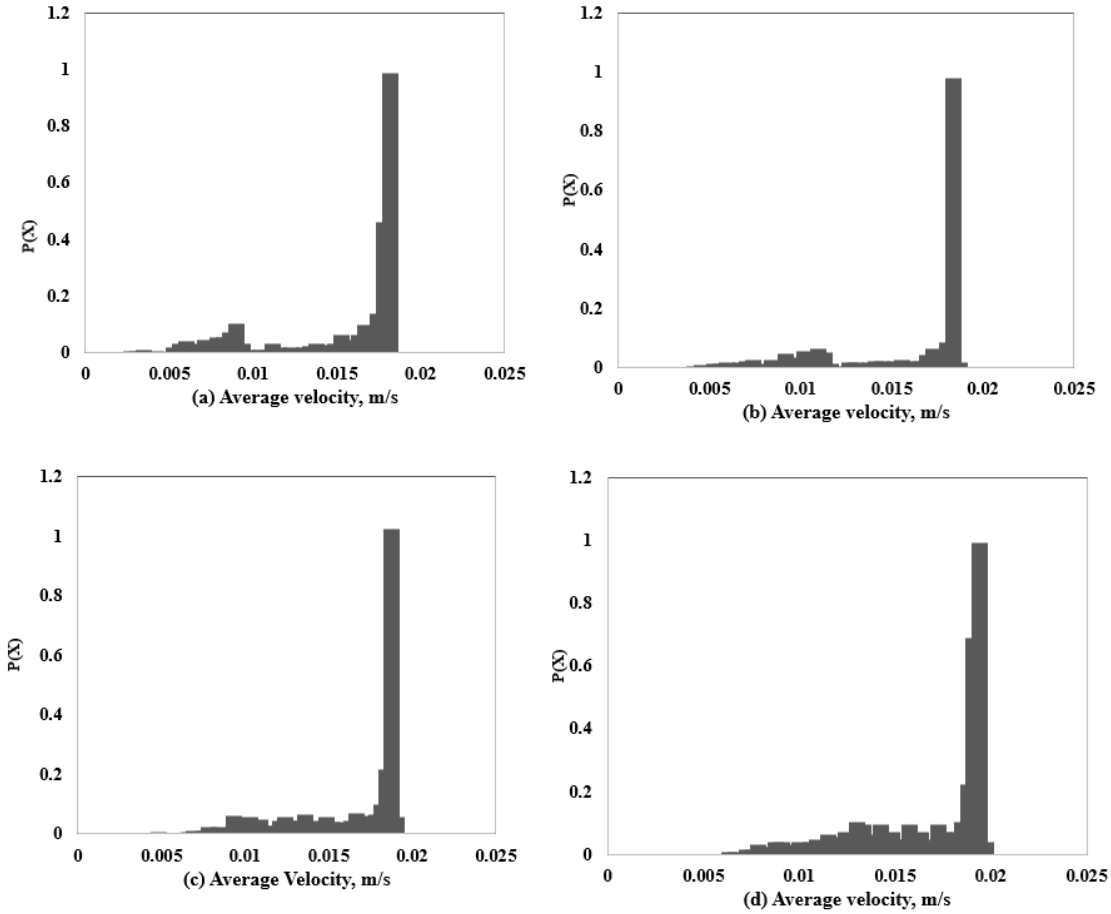

Figure 5: Average velocity magnitude: (a) 10 g, (b) 15 g, (c) 20 g and (d) 25 g of beads

Increasing the surface area of accessible beads enhances CNT interaction and deposition, thereby boosting CNT synthesis. This favourable environment provides more suitable growth sites for CNT formation, thereby increasing production rate. However, exceeding 10 g of bead mass unexpectedly reduces the production rate. Stationary particles likely contribute to overcrowding due to poor interactions from agglomeration, and as beads become more densely packed, the conditions for CNT growth deteriorate. This is probably caused by decreased surface accessibility from overlapping or tighter packing, which impedes carbon precursor access during CNT synthesis. [22-24].

4.4 Methane Concentration

A histogram of the average methane concentration for all bead masses is shown in Figure 6. The highest methane distribution was observed in the region with the highest temperature at 10 g of beads, as shown in Figure 6(a), while the lowest distribution was seen in Figure 6(d) at 25 g of beads. Additionally, increased fluidization can displace methane, which is the primary carbon precursor and a major contributor to CNT growth. This displacement can lower methane levels, and enhanced gas mixing due to fluidization likely reduced the

local concentration of the carbon precursor, thereby hindering methane's role in CNT growth.

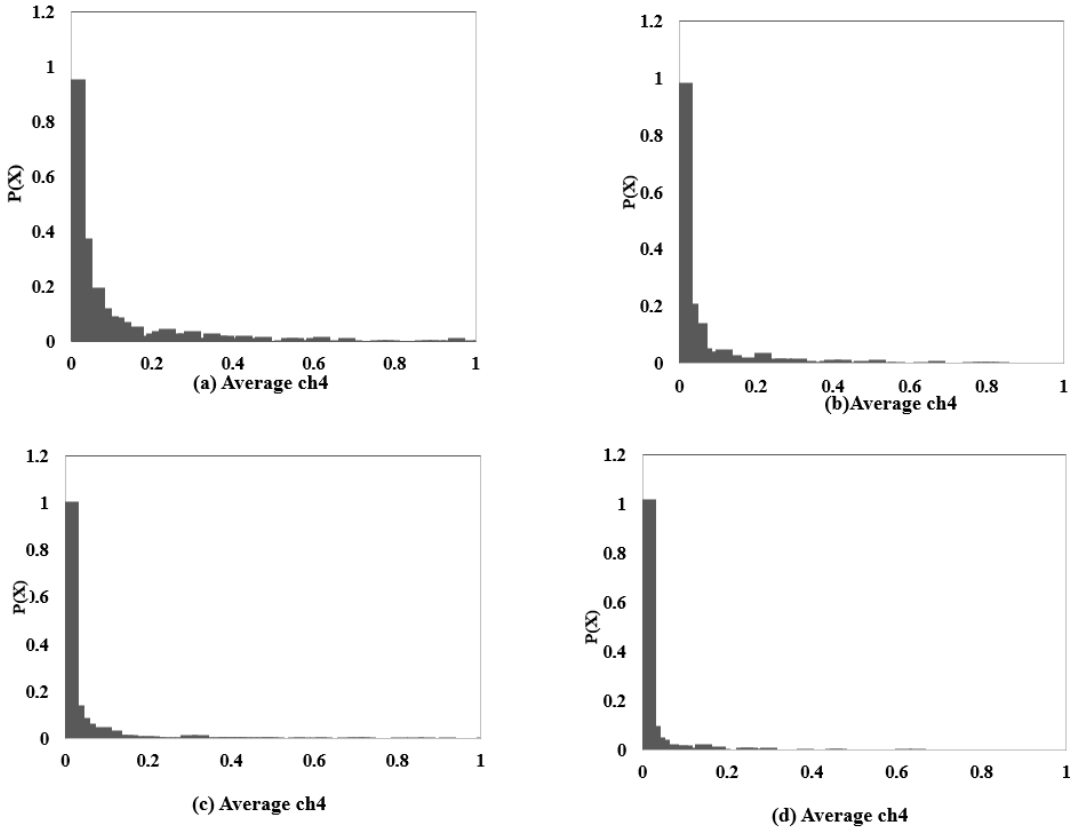

Figure 6: Methane distribution (a) 10 g, (b) 15 g, (c) 20 g, (d) 25 g of beads

Fluidization can also reduce the residence time of carbon precursors in the reaction zone, potentially limiting their role in CNT formation. [25-27]. Catalyzed particles often become deactivated when high carbon concentrations in the precursor encapsulate the catalyst metal particles, thereby preventing them from facilitating further carbon deposition. This encapsulation occurs when excess carbon forms a thick layer around the catalyst particles, hindering their activity and stopping CNT growth. Additionally, carbon concentration affects the diffusion of the carbon source through the CNT array to reach the substrate's catalysts. Proper diffusion maintains a steady supply of carbon, supporting CNT growth. Conversely, too much or too little carbon can disrupt diffusion, impacting both the growth mechanism and the efficiency of CNT synthesis. [28,29]. The high-temperature regime with 10 g of beads accelerates methane decomposition, increasing carbon diffusion and resulting in a higher growth rate. In Figure 6, methane decomposition was highest with 10 g of beads, confirming the higher growth rate of 1.2 observed in Figure 4. The increased carbon diffusion rate in this scenario required substantial consumption of the carbon feedstock for CNT synthesis.

4.5 Temperature distribution

Figure 7 shows the distribution of the average growth temperature at all bead masses under study. The highest temperature is 1200 K in the 10 g case, as shown in Figure 7(a), while the lowest temperature is observed with 25 g of beads, as shown in Figure 7(d). As fluidization increases, the temperature distribution decreases, and the mass of beads increases. The flow of nitrogen gas controls the intensity of fluidization; as the nitrogen

flow rate increases, fluidization is enhanced. In this study, the nitrogen flow rate increases with increasing bead mass, as shown in Figure 7. Inert gases such as nitrogen have a high relative specific heat capacity, making them effective cooling agents. Fluidization is intensified by the increased nitrogen flow rate, which absorbs a substantial amount of heat generated during CNT growth**.**

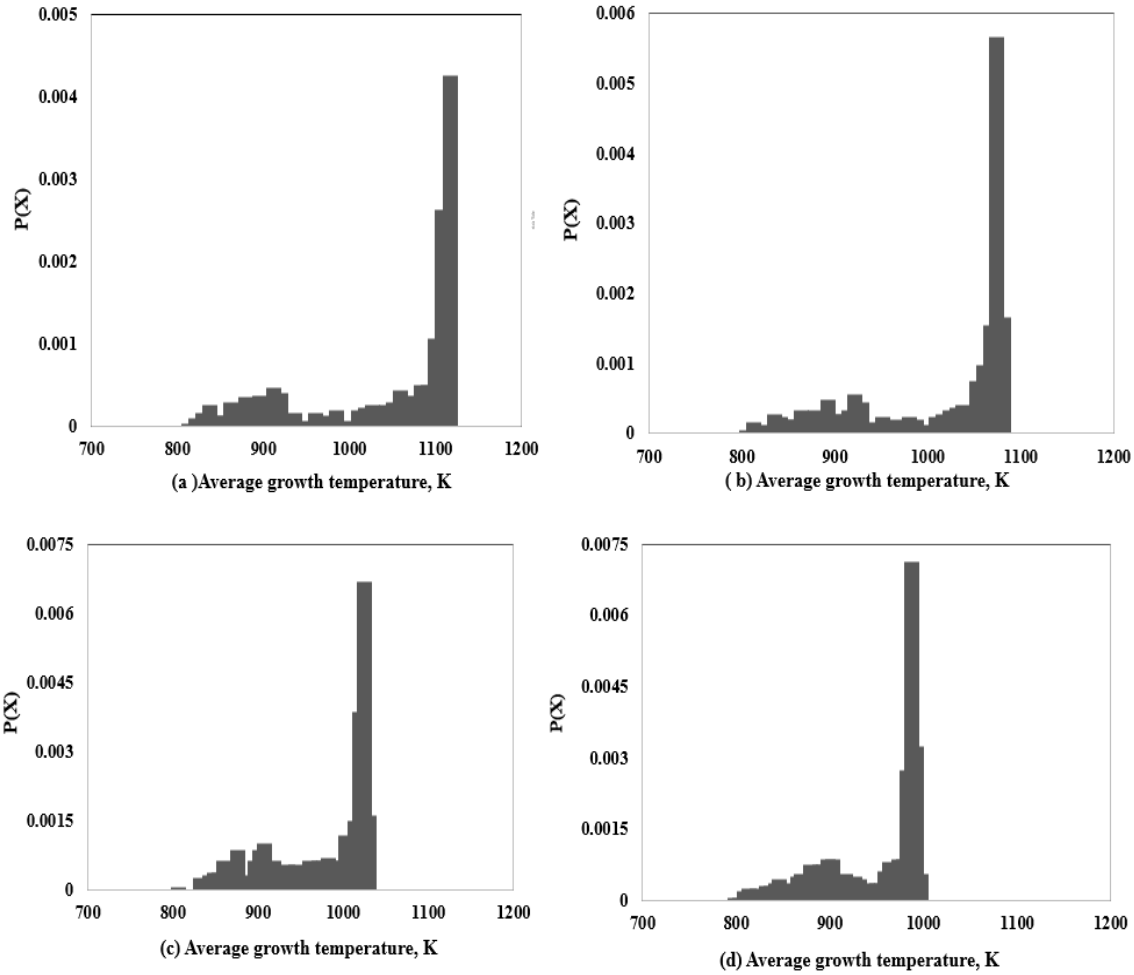

Figure 7: Average growth temperature (a) 10 g, (b) 15 g, (c) 20 g, and (d) 25 g.

Absorbed heat effectively lowers the growth temperature during CNT synthesis, leading to a significant decrease in growth rate from smaller beads (10 g) to larger beads (25 g). Additionally, the size of CNTs is closely linked to the diameter of the catalyst particles on which they grow, which is influenced by the carbon concentration. Higher temperature profiles lead to higher levels of carbon precursors, producing larger catalyst particles and thicker CNTs, whereas lower temperatures yield smaller particles and thinner CNTs [14, 26, 27].

Excessive bead mass can cause uneven heat and reactant gas distribution within the growth chamber. This uneven distribution leads to localized cooling, hindering efficient CNT growth. A larger bead mass also restricts the movement of carbon precursors, reducing the effective concentrations of methane and other reactants. Additionally, increasing bead mass worsens thermal management issues. Heating a larger volume of material becomes more difficult, potentially creating temperature gradients that affect the uniformity and quality of CNT growth at catalyst sites [30-32]. The influence of temperature is clearly evident, showing that temperature is the main factor affecting production rates.

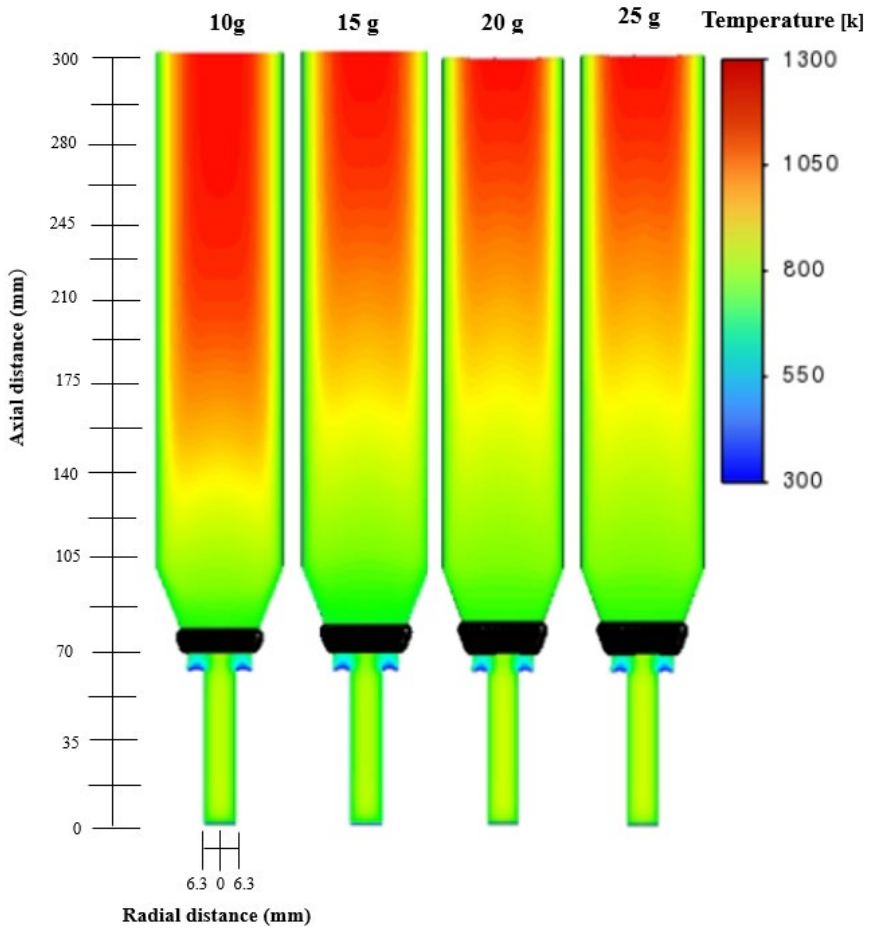

Figure 8: Contour of the temperature profile of the CNT synthesis for the five cases of (a) 10 g, (b) 15 g, (c) 20 g, and (d) 25 g.

As shown in Figure 8, the temperature decreases with increasing bead mass. This trend is evident in Figure 7, where the temperature ranges from 500°C to the maximum furnace temperature of 1300°C, along with the flame-assisted chemical vapor deposition (FCVD) flame temperature distribution. The increase in nitrogen flow rate, which controls fluidization intensity, is also clearly visible, leading to a decrease in temperature within the flow domain during the growth process. Figure 8 displays temperature contours of the growth rate profile from 10 g to 25 g. Significantly, the temperature drops as the bead mass increases.

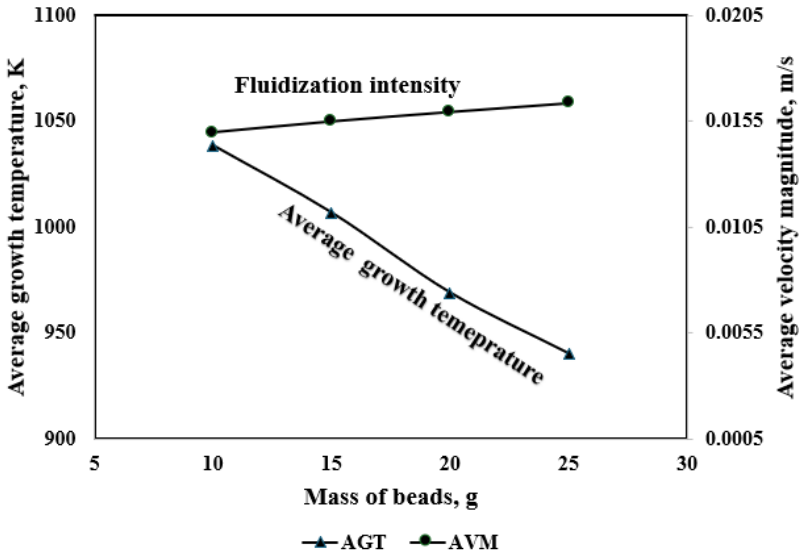

Figure 9: Plot of the average velocity magnitude and growth temperature

Figure 9 displays the average velocity magnitude and average growth temperature, showing how the former influences particle movement and, seemingly, controls the fluidization intensity. Fluidization increases markedly from 10 g to 25 g of beads, which explains the drop in the temperature profile between these two masses, as fluidization affects the temperature. The velocity magnitude, which indicates the fluidization strength, remains roughly constant across the four cases, suggesting that fluidization has little effect on the carbon nanotube production rate. However, the average growth temperature continues to decline due to the cooling effect of the flowing nitrogen gas in the fluidization medium as the bead mass increases. This temperature behaviour also indicates that the CNT production rate mainly depends on the temperature regime.

Although the fluidization may not be strong enough to move some particles at higher masses, the increase still causes a drop in both temperature and methane concentration, the primary carbon precursor crucial for CNT growth. Additionally, the growth temperature drops with the introduction of nitrogen cold flow, due to enhanced fluidization. Ineffective fluidization can cause bead particles to agglomerate as the bead mass increases, reducing substrate surface area and limiting CNT growth sites. Increased nitrogen flow rates from fluidization may also lower the optimal temperature for CNT growth, thus decreasing production rates. Conversely, at lower bead masses (10 g), fluidization is sufficient to spread the bead surface area, providing ample growth sites for CNT formation. However, as agglomeration progresses and bead masses increase, access to growth sites becomes increasingly restricted for precursors, reducing the amount of carbon reaching them and ultimately lowering production rates. At 10 g, production rates improve due to adequate fluidisation, which provides an optimal surface area for CNT growth [20, 23, 26]. However, a decline in the production rate occurs from 15 g in Figure 9 downwards, accompanied by a decrease in temperature and reduced accessibility of carbon precursors, as shown in Figure 6.

5.0 CONCLUSION

The predicted production rate aligns well with the experimental results at 10 and 25 g. A 13% overprediction in production rate was noted compared to the other two cases. It is expected that the production rate will increase as fluidization and bead mass continue to

rise, which are necessary for expanding the substrate surface area and particle mobility; however, the opposite occurs. The decrease in temperature suggests that increased fluidization, involving nitrogen cold flow, may be responsible for the temperature reduction. It is also known that a suitable and favorable temperature environment is required for CNT formation and growth; therefore, the decline in temperature may explain the low production rate as fluidization and bead mass increase. Additionally, fluidization effects influence methane composition: increased fluidization leads to lower temperature and thus reduced methane concentration. The rise in bead mass also causes particle agglomeration, resulting in overlaps that hinder access of carbon precursors to the CNT growth sites. Some of the findings mentioned above were not observable during the experimental process. Finally, it is clear that the growth rate, which mainly depends on the source temperature, is a key factor in determining production rate. Therefore, it can be concluded that the growth rate depends on the production rate, and it was ultimately established that for every 1 mg of CNTs, there will be 2.613 µm of CNT length.

ACKNOWLEDGEMENT

The research was funded by Universiti Teknologi Malaysia (UTM) through the UTM Fundamental Research (UTMFR: PY/2024/01611) grant with cost centre number Q.J130000.3824.23H94. This research was also supported by Universiti Teknologi Malaysia (UTM) through the Prototype Development Fund (PDF Cycle 2: PY/2024/00430) grant with cost centre number Q.J130000.4424.4J676.

REFERENCE

[1] M. T. Zainal *et al.*, “Zero-dimensional model for the prediction of carbon nanotube (CNT) growth region in heterogeneous methane-flame environment,” *Carbon Lett.*, vol. 33, no. 7, pp. 2199–2210, 2023, doi: 10.1007/s42823-023-00579-z.

[2] Muhammad Syafiq Ridhwan Selamat, Muhammad Thalhah Zainal, Mohd Fairus Mohd Yasin, Norikhwan Hamzah, and Nor Azwadi Che Sidik, “Modelling of the Flame Synthesis of Single-walled Carbon Nanotubes in Non-premixed Flames with Aerosol Catalyst,” *J. Adv. Res. Numer. Heat Transf.*, vol. 13, no. 1, pp. 39–51, 2023, doi: 10.37934/arnht.13.1.3951.

[3] H. Norikhwan, “Carbon Nanotube Growth Region Characterization Using Wire-Based Macro-Imaging Method Norikhwan Hamzah Universiti Teknologi Malaysia,” pp. 0–200, 2020.

[4] W. Liu, D. Liu, Y. Zhang, and B. Li, “Numerical investigation of particle size distribution, particle transport and deposition in a modified chemical vapour deposition process,” *Powder Technol.*, vol. 407, p. 117616, Jul. 2022, doi: 10.1016/j.powtec.2022.117616.

[5] G. P. Gakis, S. Termine, A. F. A. Trompeta, I. G. Aviziotis, and C. A. Charitidis, “Unravelling the mechanisms of carbon nanotube growth by chemical vapour deposition,” *Chem. Eng. J.*, vol. 445, Oct. 2022, doi: 10.1016/j.cej.2022.136807.

[6] N. Baig, I. Kammakakam, W. Falath, and I. Kammakakam, “Nanomaterials: A review of synthesis methods, properties, recent progress, and challenges,” *Mater. Adv.*, vol. 2, no. 6, pp. 1821–1871, 2021, doi: 10.1039/d0ma00807a.

[7] N. Abid *et al.*, “Synthesis of nanomaterials using various top-down and bottom-up approaches, influencing factors, advantages, and disadvantages: A review,” *Adv. Colloid Interface Sci.*, vol. 300, no. December 2021, 2022, doi: 10.1016/j.cis.2021.102597.

[8] M. D. Rezaee, B. Dahal, J. Watt, M. Abrar, D. R. Hodges, and W. Li, “Structural, Electrical, and Optical Properties of Single-Walled Carbon Nanotubes Synthesised through Floating Catalyst Chemical Vapour Deposition,” 2024.

[9] L. von Berg, A. Anca-Couce, C. Hochenauer, and R. Scharler, “Multi-scale modelling of fluidized bed biomass gasification using a 1D particle model coupled to CFD,” *Fuel*, vol. 324, no. March, 2022, doi: 10.1016/j.fuel.2022.124677.

[10] W. J. Sawyer and A. J. Hart, “Aerosol synthesis of high-quality single-wall carbon nanotubes through integrated microplasma generation of catalyst nanoparticles,” *Chem. Eng. J.*, vol. 507, no. October 2024, p. 160690, 2025, doi: 10.1016/j.cej.2025.160690.

[11] M. S. Challiwala, G. Ibrahim, H. A. Choudhury, and N. O. Elbashir, “Scaling up the advanced dry reforming of methane (DRM) reactor system for multi-walled carbon nanotubes and syngas production: An experimental and modelling study,” *Chem. Eng. Process. - Process Intensif.*, vol. 197, no. February, p. 109693, 2024, doi: 10.1016/j.cep.2024.109693.

[12] M. Liu, M. Wang, K. Zhang, and H. Yu, "Simulation of synthesising carbon nanotubes by catalytic chemical vapour deposition in a fluidized bed using a CFD-PBM model," *Powder Technol.*, vol. 457, p. 120927, 2025, doi: https://doi.org/10.1016/j.powtec.2025.120927.
[13] M. T. Zainal, M. F. Mohd Yasin, W. F. F. Wan Ali, K. F. Tamrin, and M. H. Ani, "Carbon precursor analysis for catalytic growth of carbon nanotube in flame synthesis based on semi-empirical approach," *Carbon Lett.*, vol. 30, no. 5, pp. 569–579, 2020, doi: 10.1007/s42823-020-00127-z.
[14] T. O. Cabral, P. B. Amama, and D. B. Pourkargar, "Multiscale-multiphysics predictive modelling of chemical vapour deposition processes for carbon nanotube synthesis," *Chem. Eng. Sci.*, vol. 305, no. December 2024, p. 121137, 2025, doi: 10.1016/j.ces.2024.121137.
[15] B. Safaei, H. C. How, and G. Scribano, "A computational study on synthesis of carbon nanotubes in a sooty inverse diffusion flame," *Int. J. Environ. Sci. Technol.*, vol. 20, no. 3, pp. 1–10, 2023, doi: 10.1007/s13762-022-04143-6.
[16] B. Leclaire *et al.*, "First challenge on Lagrangian Particle Tracking and Data Assimilation: datasets description and planned evolution to an open online benchmark," *14th Int. Symp. Part. Image Velocim.*, vol. 1, no. 1, 2021, doi: 10.18409/ispiv.v1i1.119.
[17] A. Sciacchitano, B. Leclaire, and A. Schroeder, "Main results of the first Lagrangian Particle Tracking Challenge," *14th Int. Symp. Part. Image Velocim.*, vol. 1, no. 1, 2021, doi: 10.18409/ispiv.v1i1.197.
[18] Y. W. Son, C. O. Ahn, and S. H. Lee, "Using a Lagrangian-Lagrangian approach for studying flow behaviour inside a bubble column," *Nucl. Eng. Technol.*, vol. 55, no. 12, pp. 4395–4407, 2023, doi: 10.1016/j.net.2023.08.018.
[19] C. Kehl, P. D. Nooteboom, M. L. A. Kaandorp, and E. van Sebille, "Efficiently simulating Lagrangian particles in large-scale ocean flows—Data structures and their impact on geophysical applications," *Comput. Geosci.*, vol. 175, no. July 2022, p. 105322, 2023, doi: 10.1016/j.cageo.2023.105322.
[20] H. A. Kafiabad, "Grid-based calculation of the Lagrangian mean," *J. Fluid Mech.*, vol. 940, no. Lm, pp. 1–20, 2022, doi: 10.1017/jfm.2022.233.
[21] F. Petrosino, D. de Rosa, and G. Mingione, "Application of different Lagrangian particle tracking techniques for water impingement," *IOP Conf. Ser. Mater. Sci. Eng.*, vol. 1024, no. 1, 2021, doi: 10.1088/1757-899X/1024/1/012011.
[22] M. T. Zainal, M. F. Mohd Yasin, W. F. F. Wan Ali, K. F. Tamrin, and M. H. Ani, "Carbon precursor analysis for catalytic growth of carbon nanotube in flame synthesis based on semi-empirical approach," *Carbon Lett.*, vol. 30, no. 5, pp. 569–579, 2020, doi: 10.1007/s42823-020-00127-z.
[23] "FLAME STRUCTURE EFFECTS ON CARBON NANOTUBE GROWTH REGION".
[24] B. Yang *et al.*, "Experimental and simulation research on the preparation of carbon nano-materials by chemical vapour deposition," *Materials (Basel),* vol. 14, no. 23, 2021, doi: 10.3390/ma14237356.
[25] M. D. Ahmad Termizi, "Growth of Carbon Nanotubes on Spherical Substrate Using Biogas Premixed Flame With Direct Vaporisation Technique," 2021.
[26] M. T. Zainal *et al.*, "Zero-dimensional model for the prediction of carbon nanotube (CNT) growth region in heterogeneous methane-flame environment," *Carbon Lett.*, pp. 1–19, 2023, doi: 10.1007/s42823-023-00579-z.
[27] M. P. Bondarde *et al.*, "Carbon-based anode materials for lithium-ion batteries," *Lithium-Sulphur Batter. Mater. Challenges Appl.*, vol. 114, pp. 521–545, 2022, doi: 10.1016/B978-0-323-91934-0.00004-1.
[28] W. Shi *et al.*, "Synthesis Mechanisms, Structural Models, and Photothermal Therapy Applications of Top-Down Carbon Dots from Carbon Powder, Graphite, Graphene, and Carbon Nanotubes," *Int. J. Mol. Sci.*, vol. 23, no. 3, 2022, doi: 10.3390/ijms23031456.
[29] W. Bai, D. Chu, and Y. He, "Fluidisation dynamic characteristics of carbon nanotube particles in a tapered fluidized bed," *Chinese J. Chem. Eng.*, vol. 44, pp. 321–331, Apr. 2022, doi: 10.1016/j.cjche.2021.03.006.
[30] H. J. Basheer, K. Baba, and N. Bahlawane, "Thermal Chemical Vapour Deposition of Superblack Randomly Orientated Carbon Nanotube Coatings," vol. 1900704, pp. 1–6, 2020, doi: 10.1002/pssa.201900704.
[31] M. Li, M. Risa, T. Osawa, H. Sugime, and S. Noda, "Facile catalyst deposition using mist for fluidized-bed production of sub-millimetre-long carbon nanotubes," *Carbon N. Y.*, vol. 167, pp. 256–263, 2020, doi: 10.1016/j.carbon.2020.06.018.
[32] R. Dubey, D. Dutta, A. Sarkar, and P. Chattopadhyay, "Functionalised carbon nanotubes: synthesis, properties and applications in water purification, drug delivery, and material and biomedical sciences," *Nanoscale Adv.*, vol. 3, no. 20, pp. 5722–5744, 2021, doi: 10.1039/d1na00293g.